

The $(n, 2n)$ reaction for the lightest stable erbium isotope ^{162}Er from reaction threshold up to 19 MeV

E. Georgali,¹ Z. Eleme,¹ N. Patronis,¹ X. Aslanoglou,¹ M. Axiotis,² M. Diakaki,³ V. Foteinou,² S. Harissopoulos,² A. Kalamara,⁴ M. Kokkoris,⁴ A. Lagoyannis,² N. G Nicolis,¹ G. Provas,² A. Stamatopoulos,⁴ S. Stoulos,⁵ A. Tsinganis,^{4,6} E. Vagena,⁵ R. Vlastou,⁴ and S. M. Vogiatzi¹

¹Department of Physics, University of Ioannina, 45110 Ioannina, Greece

²Tandem Accelerator Laboratory, Institute of Nuclear and Particle Physics, N.C.S.R. "Demokritos", Aghia Paraskevi, 15310 Athens, Greece

³CEA/Saclay-IRFU, Gif-sur-Yvette, France

⁴Department of Physics, National Technical University of Athens, Zografou Campus, 15780 Athens, Greece

⁵Department of Physics, Aristotle University of Thessaloniki, 54124 Thessaloniki, Greece

⁶European Organization for Nuclear Research (CERN), Geneva, Switzerland



(Received 27 March 2018; revised manuscript received 25 May 2018; published 26 July 2018)

The $^{162}\text{Er}(n, 2n)^{161}\text{Er}$ reaction cross section ($E_{th} = 9.26$ MeV) was measured at six incident neutron beam energies by means of the activation technique. Two energy regions were covered in the present work: the near-threshold energies between 10.7 and 11.3 MeV, as well as the higher energies from 17.1 up to 19.0 MeV. In this way, the energy range from the reaction threshold up to 19 MeV was experimentally mapped, considering also the existing experimental information around 14 MeV. The quasi-monoenergetic neutron beam at near-threshold energies was produced via the $^2\text{H}(d, n)^3\text{He}$ reaction, while the higher neutron beam energies were achieved by using the $^3\text{H}(d, n)^4\text{He}$ reaction. The primary deuteron beam was delivered in both cases by the 5.5 MV Tandem Van de Graaff accelerator of NSCR "Demokritos." Statistical model calculations were performed and compared with all the available experimental data.

DOI: [10.1103/PhysRevC.98.014622](https://doi.org/10.1103/PhysRevC.98.014622)

I. INTRODUCTION

Neutron induced threshold reactions are in general of special interest for basic research purposes, as well as for the development of nuclear physics applications.

In recent years innovative fast neutron reactor designs have been proposed for burning fissile isotopes that can be constituents of the existing nuclear waste, while at the same time nuclear energy can be produced [1,2]. Towards this direction, the upgrading of the existing nuclear data libraries with accurate experimental information in the fast neutron energy region is of primary importance. Accordingly, detailed studies are needed on isotopes and reactor structural materials that affect the neutron economy. Rare-earth isotopes are of special interest in nuclear technology, not only as fuel structural materials [3], but also as candidate neutron absorbers. In particular erbium isotopes can be used as burnable poisons in several reactor designs (e.g., [4,5]).

A second reason for carrying out the present work originates from the fact that the existing experimental information is limited to neutron beam energies around 14 MeV [6–14].

In order to validate the theoretical estimations and improve the parametrization of the statistical model calculations, the experimental mapping of the $^{162}\text{Er}(n, 2n)^{161}\text{Er}$ excitation function is needed for an extended energy region. For this reason, within the present work the $^{162}\text{Er}(n, 2n)^{161}\text{Er}$ reaction cross section was studied, for the first time, at near-threshold energies between 10.7 and 11.3 MeV, as well as at higher energies from 17.1 up to 19.0 MeV. The experimental information at near-threshold energies is crucial for testing the performance of the theoretical calculations by defining the steepness of the slope of the excitation function. The higher neutron energy region considered in the present work is also important for two reasons: the role of the $(n, 3n)$ reaction channel has to be investigated, along with the contribution of the pre-equilibrium mechanism to the observed reaction rate.

The experimental study of the $^{162}\text{Er}(n, 2n)^{161}\text{Er}$ reaction is a challenging procedure due to the fact that, among the six stable erbium isotopes, ^{162}Er is the lightest one [15], with a natural abundance of $\sim 0.14\%$ (see Table I). Therefore, special experimental conditions should be applied in order to achieve reasonable statistical accuracy for the cross section measurements, as described below.

In the following sections, experimental results are discussed and compared with statistical model calculations performed by the following codes: TALYS (v. 1.8) [16], EMPIRE (v. 3.2.2) [17], and MECO [18].

Published by the American Physical Society under the terms of the [Creative Commons Attribution 4.0 International](https://creativecommons.org/licenses/by/4.0/) license. Further distribution of this work must maintain attribution to the author(s) and the published article's title, journal citation, and DOI.

TABLE I. Natural abundances of the erbium isotopes [15].

Erbium isotope	Natural abundance (%)
^{162}Er	0.139 ± 0.005
^{164}Er	1.601 ± 0.003
^{166}Er	33.503 ± 0.036
^{167}Er	22.869 ± 0.009
^{168}Er	26.978 ± 0.018
^{170}Er	14.910 ± 0.036

II. EXPERIMENT

1. Irradiations

The $^{162}\text{Er}(n, 2n)^{161}\text{Er}$ reaction cross section was measured in two energy ranges: near the reaction threshold, at energies of 10.7, 11.0, and 11.3 MeV and at higher energies of 17.1, 18.1, and 19.0 MeV. In all cases, the activation technique was applied. The neutron beam intensity for the cross section measurements was determined by using the following reference reactions: $^{27}\text{Al}(n, \alpha)^{24}\text{Na}$, $^{197}\text{Au}(n, 2n)^{196}\text{Au}$, and $^{93}\text{Nb}(n, 2n)^{92m}\text{Nb}$ [19]. The irradiations were performed at the 5.5 MV Tandem Van de Graaff accelerator of NCSR “Demokritos.” Each irradiation lasted for ~ 10 h, corresponding to $\sim 85\%$ of the saturated activity of the product nucleus.

Two erbium samples of ~ 1 g each were prepared. The samples consisted of a mixture of 90% Er_2O_3 powder of natural composition (with purity $\geq 99.99\%$) and 10% of cellulose pulver to improve the mechanical properties of the sample. The mixture was pressed to form a pellet of 2 mm thickness and 13 mm diameter. During the irradiations each erbium sample was sandwiched between monitor foils (Al, Nb, and Au) of equal diameter.

The three lower neutron beam energies were produced via the $^2\text{H}(d, n)^3\text{He}$ reaction ($Q = 3.269$ MeV) by bombarding a D_2 gas target [20] with a deuteron beam current of 2–3 μA . A molybdenum foil with 5 μm thickness served as the entrance window and a Pt foil as the beam stop of the gas cell. During the irradiations the gas target was cooled via a cold air jet to minimize the effect of heating in the deuterium gas pressure, which was continuously controlled via a micrometric valve. In this way, the gas pressure was kept constant at 1250 mbar. The samples were placed at 0° with respect to the primary deuteron beam and at 7 cm distance from the center of the gas cell. With this configuration the angular acceptance of the samples was lower than 5° and the neutron flux during the irradiations varied between 3.0×10^5 and 2.1×10^6 $n/(\text{cm}^2 \text{ s})$.

The irradiations at higher neutron beam energies were performed by means of the $^3\text{H}(d, n)^4\text{He}$ reaction ($Q = 17.59$ MeV). The deuterons were accelerated to energies higher than 2.5 MeV in order to keep the transmission efficiency of the accelerator within affordable limits, given that for lower beam energies the beam transmission efficiency seriously deteriorates. The beam energy was degraded by using two molybdenum foils, 5 μm thick each, placed in front of a 2.1 mg/cm^2 Ti-tritiated target. The Ti-tritiated target was on top of a 1 mm thick Cu backing for optimum heat conduction purposes. The target flange was air cooled during the

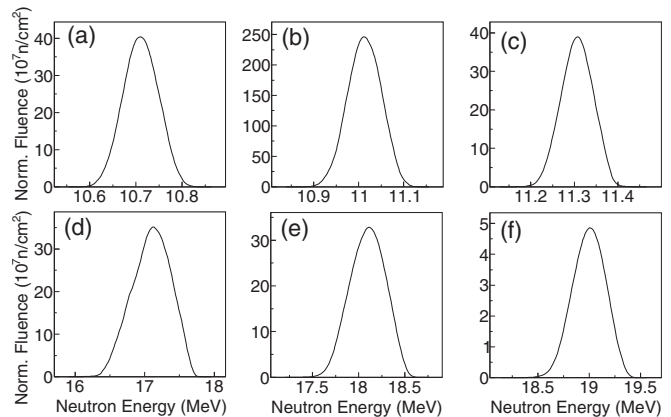


FIG. 1. Neutron energy spectra calculated with NEUSDESC code [21] for the adopted irradiation setup geometry: (a) 10.7 ± 0.1 MeV, (b) 11.0 ± 0.1 MeV, (c) 11.3 ± 0.1 MeV, (d) 17.1 ± 0.3 MeV, (e) 18.1 ± 0.2 MeV, and (f) 19.0 ± 0.2 MeV.

irradiations. The samples were placed at 0° with respect to the deuteron beam and at 2 cm distance from the Ti-tritiated target. A shorter tritium-to-sample distance was adopted in these irradiations, considering that the energy spread of the beam is less sensitive to the angular acceptance of the sample due to the reaction kinematics. The obtained neutron beam intensity in the high energy irradiations varied between 2.6×10^4 and 3.4×10^5 $n/(\text{cm}^2 \text{ s})$.

In all cases, the neutron beam energy distribution was calculated using the NEUSDESC code, developed at JRC-Geel [21]. The energy loss, the angular straggling, and the energy straggling of the deuteron beam in the structural materials of the primary target were considered by incorporating the SRIM-2008 Monte Carlo simulation program [22]. The results of the NEUSDESC code [21] were also compared and validated with other computer codes (e.g., CONY, Computer cODE for Neutron Yield calculations [23]). The possible influence on the neutron beam energy distribution originating by neutron scattering within target structural materials was investigated by Kalamara [24] by combining the results of the NEUSDESC code [21] with MCNP5 Monte Carlo simulations [25]. For both target configurations it was concluded that the neutron scattering is negligible. The neutron beam energy distribution for the six energies is presented in Fig. 1.

During the irradiations, the neutron beam was monitored by a BF_3 detector, placed at a 3 m distance from the target configuration. The counting rate of the BF_3 detector was recorded every 60 s by means of a multichannel scaler and was used for the accurate estimation of the decay rate of the product nuclei during the irradiations. In this way the fluctuations of the neutron beam intensity were taken into account in the data analysis.

The main quantities concerning the irradiations of the samples are summarized in Table II.

2. Activity measurements

Following the irradiations, the induced activity of the erbium sample was measured using two 100% relative efficiency high-purity germanium (HPGe) detectors. The two detectors

TABLE II. Summary of the irradiation parameters.

	10.7 MeV	11.0 MeV	11.3 MeV	17.1 MeV	18.1 MeV	19.0 MeV
Irradiation time (h)	9.95	9.88	10.10	10.07	10.00	9.98
Integrated flux ($\times 10^{10} \text{ cm}^{-2}$)	1.29 ± 0.09	7.50 ± 0.53	1.09 ± 0.08	1.23 ± 0.09	1.07 ± 0.07	0.95 ± 0.07
Measuring time (h)	4.00	10.11	5.12	10.01	5.00	7.01
Decay correction f_B for erbium target	0.387	0.404	0.416	0.414	0.397	0.392

were placed face to face in close geometry (Fig. 2). The distance between the detector windows was 22 mm. The sample was placed in the midspace of the two HPGe detectors, centered on their common axis. The absolute peak efficiency of this setup for the stronger decay line of ^{161}Er at 826.6 keV [26] was $\epsilon_\gamma = (10.5 \pm 0.4)\%$. The high detection efficiency of the γ spectrometer was a critical factor for accumulating satisfactory statistics from the weak induced activity of the erbium sample, given the minimal abundance (0.139%) of ^{162}Er in the natural composition sample. The duration of the measurement of the erbium sample activity, as given in Table II, was adjusted to achieve the minimum possible statistical uncertainty according to the peak-to-background counting rate ratio.

It has to be mentioned that despite the close detection geometry and the complexity of the decay scheme of ^{161}Er [26], coincidence summing effects are not expected for the 826.6 keV line. Specifically, the summing-in and summing-out possible effects were calculated according to the method described by Debertain and Helmer [27]. In these calculations for the 826.6 keV decay line, the decay scheme of ^{161}Er [26] was taken into account, where the total and peak-efficiency for the adopted detection geometry was deduced through GEANT4 Monte Carlo calculations [28]. In all cases, the correction factor was found to be negligible.

For such a close geometry, the efficiency calibration of the detectors had to be performed with caution to avoid coincidence summing effects. For this reason a calibrated weak monoenergetic ^{54}Mn point source was used. The ^{54}Mn source decays through electron capture to ^{54}Cr that consequently decays to the ground state by emitting a single γ ray with energy 835 keV [29]; very close to the 826.6 keV energy of the strongest decay line of ^{161}Er . Before the measurements the

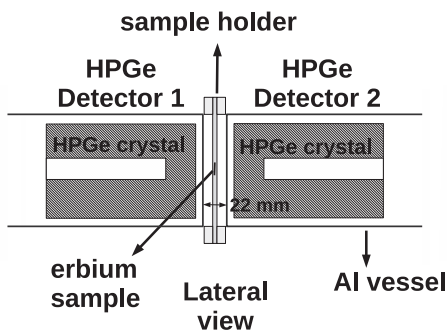


FIG. 2. Setup of the two 100% relative efficiency HPGe detectors. By adopting such a close detection geometry, the detection efficiency was maximized so as to compensate for the minimal abundance (0.139%) of the natural composition of the erbium sample with respect to the ^{162}Er isotope.

two 100% HPGe detectors were very carefully gain-matched. In this way, the addition of the two γ -ray spectra was possible for the actual γ -ray measurement, as well as for the efficiency calibration through the ^{54}Mn source. Figure 3 shows the γ -ray spectra of the erbium sample resulting from a 7 h measurement following the 17.1 MeV irradiation.

The activity of the monitor foils was measured with two 16% relative efficiency HPGe detectors: one for the lower neutron beam energies and one for the higher ones. The source to detector window distance was 7 cm. At this distance any corrections for pileup or coincidence summing effects were negligible, considering also the small relative efficiency of the detector. The absolute efficiency of the detector for the reference foil measurements was obtained using a calibrated ^{152}Eu [30] point source placed at the same sample to detector window distance.

The decay data of the reference [31–33] and erbium targets [26] are presented in Table III.

III. DATA ANALYSIS

For each run the integrated neutron flux during the irradiation of the erbium sample was measured via the activity induced at the front and back monitor foils. The total number of activated nuclei at the end of the irradiation could be derived using the following equation:

$$A = \frac{NC_A C_{DT}}{(1 - e^{-\lambda t_m}) e^{-\lambda t_w} \epsilon I}, \quad (1)$$

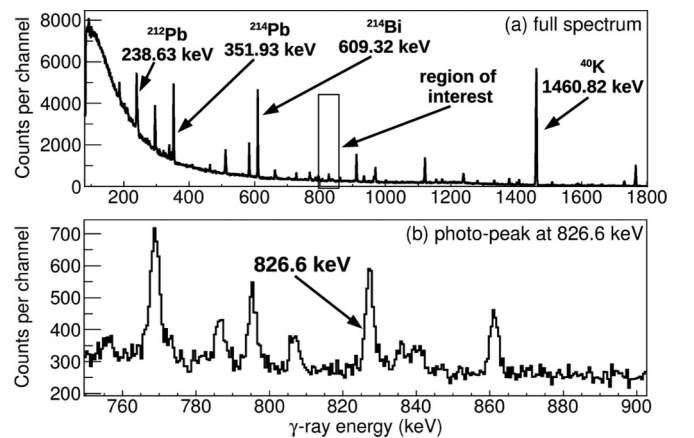


FIG. 3. The γ -ray spectra of the 17.1 MeV run. The upper panel corresponds to the full spectrum and the lower one to the region around the 827 keV line; the stronger decay line of ^{161}Er .

TABLE III. Decay properties of the product-nuclei.

Product nucleus	Half-life	γ -ray energy (keV)	Intensity per decay (%)
^{161}Er [26]	(3.21 ± 0.03) h	826.6	64.05 ± 3.70
^{24}Na [31]	(14.997 ± 0.012) h	1368.626	99.9936 ± 0.0015
^{196}Au [32]	(6.1669 ± 0.0006) d	333.03	22.881 ± 0.946
^{92m}Nb [33]	(10.15 ± 0.02) d	934.44	99.15

where N is the recorded number of counts in the decay line of the corresponding product nuclei. The factors C_A , C_{DT} correspond to the self-attenuation and dead-time corrections, respectively. The measuring time and the time interval between the end of the irradiation and the beginning of the measurement are denoted as t_m and t_w . The factors λ and I correspond to the product-nucleus decay constant and the intensity of the decay transition, respectively. The factor ϵ corresponds to the absolute peak-efficiency of the HPGe detector for the γ -ray energy.

The time-integrated neutron flux Φ_{tot} for each irradiation was deduced through the combination of Eq. (1) with the well known equation

$$A = \Phi_{\text{tot}} n \sigma f_B \quad (2)$$

where n corresponds to the number of sample atoms per cm^2 , whereas σ is the cross section of the reference reaction used. In all cases, the reference reaction cross sections were taken from the IRDFF-1.05 (2014) database [19]. The time factor f_B corrects for the decay of the product nuclei during

irradiation, including the time variations of the neutron flux [34]. By averaging over the recorded neutron flux from the front and back monitor foils, the geometrical factor, as well as possible neutron scattering and shielding effects are taken into account.

The measured activity of the erbium sample, as well as the one from the reference foils were corrected for self-attenuation and for the effect of the extended geometry by means of GEANT4 [28] Monte-Carlo simulations. In these simulations all the details of the detection geometry were taken into account. The performance of the simulations was verified in all cases through the comparison with the experimental efficiency data obtained using the calibrated point sources.

By combining Eqs. (1) and (2) and by using the average neutron flux as derived from the monitor foils, the $^{162}\text{Er}(n, 2n)^{161}\text{Er}$ reaction cross section was deduced.

The corresponding uncertainties were obtained by summing up quadratically all the possible individual errors that are summarized in Table IV. As can be seen, the main

TABLE IV. Compilation of uncertainties (in %).

E_n (MeV):	10.7	11.0	11.3
Reference reaction:	$^{27}\text{Al}(n, \alpha)^{24}\text{Na}$	$^{197}\text{Au}(n, 2n)^{196}\text{Au}$	$^{93}\text{Nb}(n, 2n)^{92m}\text{Nb}$
Reference reaction cross section	1.0	2.7	1.2
Neutron flux	7.0	7.0	7.0
^{161}Er peak counting statistics	16.0	2.9	10.5
$2 \times 100\%$ HPGe detectors efficiency	3.8	3.8	3.8
^{161}Er γ -ray intensity per decay	5.8	5.8	5.8
Erbium target self-attenuation correction factor	0.5	0.5	0.5
^{162}Er natural abundance	3.6	3.6	3.6
Reference foils peak counting statistics	2.6, 3.4	2.1, 1.1	14.0, 11.8
16% HPGe detectors efficiency	2.0	1.6	1.3
Reference foils γ -ray intensity per decay	0.0015	4.1	
Reference foils self-attenuation correction factor	0.50	0.18	0.4
Total uncertainty of cross section	18.2	10.7	14.1
E_n (MeV):	17.1	18.1	19.0
Reference reaction:	$^{197}\text{Au}(n, 2n)^{196}\text{Au}$	$^{197}\text{Au}(n, 2n)^{196}\text{Au}$	$^{93}\text{Nb}(n, 2n)^{92m}\text{Nb}$
Reference reaction cross section	2.1	1.9	1.2
Neutron flux	7.0	7.0	7.0
^{161}Er peak counting statistics	5.5	7.5	7.0
$2 \times 100\%$ HPGe detectors efficiency	3.8	3.8	3.8
^{161}Er γ -ray intensity per decay	5.8	5.8	5.8
Erbium target self-attenuation correction factor	0.5	0.5	0.5
^{162}Er natural abundance	3.6	3.6	3.6
Reference foils peak counting statistics	4.6, 3.0	5.4, 6.4	7.1, 7.6
16% HPGe detectors efficiency	1.9	1.9	1.6
Reference foils γ -ray intensity per decay	4.1	4.1	
Reference foils self-attenuation correction factor	0.18, 0.13	0.13	0.4
Total uncertainty of cross section	11.2	12.5	12.0

contribution to the overall uncertainties arises from the neutron flux determination and from erbium peak-counting statistics. Given the rather extended thickness (2 mm) of the erbium sample, the dominant uncertainty factor resulted from the determination of the neutron flux. The counting statistical uncertainty varies between different measurements reflecting mainly the variations in the primary deuteron beam intensity. The significant contribution to the overall uncertainty from other systematic errors, namely the 826.6 keV peak intensity uncertainty and the ^{162}Er abundance uncertainty should also be mentioned. The erbium samples' mass and the self attenuation correction factors have only a small impact on the overall uncertainty.

IV. THEORETICAL CALCULATIONS

Within the energy region considered in this work, the dominant reaction mechanism of neutron interaction is the compound nucleus process. Theoretical calculations of the $^{162}\text{Er}(n, 2n)^{161}\text{Er}$ reaction cross section were performed with the TALYS (v. 1.8) and EMPIRE (v. 3.2.2) statistical model codes. Furthermore, calculations were performed with the Monte Carlo statistical model code MECO. The theoretical study with different codes did not aim to promote one of them with respect to the better reproduction of the experimental results, but to derive the optimum conditions for each calculation.

In the TALYS code the reaction cross sections were calculated for all possible reaction channels in order to take into account the competition among them. The compound nucleus cross section calculations were performed in the framework of the Hauser-Feshbach theory [35]. For the optical model potential the parametrization of Koning and Delaroche *et al.* [36] was used. The pre-equilibrium contribution to the $^{162}\text{Er} + n$ channel was taken into account applying the exciton model [37]. In order to take into account the γ -ray emission channel competition, the Brink-Axel model [38,39] was implemented for the γ -ray strength functions for all the transition types except for $E1$. For the $E1$ transition, the generalized Lorentzian form of Kopecky and Uhl was used [40]. For the level density calculations six different models were tested. Three of them were phenomenological: the constant temperature model [41], the back-shifted Fermi gas model [42], and the generalized superfluid model [43,44]. Additionally, theoretical calculations were performed using three microscopic models [45–47], which are incorporated in the TALYS code.

According to the constant temperature model as introduced by Gilbert and Cameron [41], the constant temperature law is implemented for the lower excitation energies, whereas for the higher energies the Fermi gas model is adopted.

In the back-shifted Fermi gas model [42] the Fermi gas expression is implemented for all the excitation energies. In this model, for the level density calculations, the TALYS code adopts the theory suggested by Grossjean and Feldmeier [48]. This theory was put into a practical form by Demetriou and Goriely [49].

The last phenomenological level density model which was implemented was the generalized Superfluid model [43,44]. This model also distinguishes between low and higher excitation energies, but not in the way suggested by the Gilbert-

Cameron formula: below an excitation energy U_c the level densities of the nucleus are characterized by a superfluid behavior, whereas above this energy the Fermi gas model is implemented.

As mentioned above, apart from the phenomenological models, three microscopic models were applied to estimate the level densities. The first of them was introduced by Goriely *et al.* [45] (microscopic model 1) and it is based on Hartree-Fock calculations on nuclei belonging to the region between the drip lines with excitation energies up to 150 MeV and spin value up to $I = 30$. The second model was suggested by Goriely *et al.* [46] (microscopic model 2) and is a combinatorial model for level densities. In this model, single-particle levels are obtained with the Hartree-Fock-Bogoliubov method, whereas collective effects are also considered. In addition, for deformed nuclei their transition to sphericity is treated with a phenomenological method. The last implemented microscopic level density model (microscopic model 3) predicts simultaneously the single-particle levels and collective properties without contribution of any phenomenological potential effect. More specifically, for deformed nuclei their transition to spherical shape, as the excitation energy increases, is taken into account by temperature-dependent Hartree-Fock-Bogolyubov calculations [50]. This model was recommended by Hilaire *et al.* [47].

For the microscopic model suggested by Hilaire *et al.* [47] (microscopic model 3), calculations were also performed by applying a Hartree-Fock-Bogolyubov model for the γ -ray strength functions [51] and the semimicroscopic potential of Bauge *et al.* [52] for the optical model. In this way, the theoretical study of the $^{162}\text{Er}(n, 2n)^{161}\text{Er}$ reaction in accordance with microscopic models, provided by the code, was possible.

The TALYS code calculates the global and local values of the parameters of the level density models by an optimization procedure [53]. In particular, the parameters are adjusted so that the level density reproduces the experimental discrete levels [54] and D_0 [55]. D_0 is the mean s -wave neutron level spacing at the neutron separation energy and it is related to the level density according to

$$\frac{1}{D_0} = \sum_{J=|I-\frac{1}{2}|}^{J=I+\frac{1}{2}} \rho(S_n, J, \Pi) \quad (3)$$

In the EMPIRE code compound nucleus reaction cross sections were calculated in the framework of the Hauser-Feshbach theory. The adopted level density formulation was based on the generalized superfluid model as described in Ref. [56]. To account for the correlation between the incident and exit channels in elastic scattering, width fluctuation corrections were implemented using the Hofmann, Richert, Tepel, and Weidenmuller model (HRTW) [57] up to an incident neutron energy of 3 MeV. Concerning γ -ray emission, the corresponding strength functions were described via the modified Lorentzian model [58] available in the RIPL-3 database [54]. The optical model parameters for the outgoing protons were also taken from RIPL-3 using the data by Koning *et al.* [36], while parameters obtained by Avrigeanu *et al.* [59] were used for the outgoing α particles. In order to choose from RIPL-3 the

TABLE V. The statistical model codes used for the $^{162}\text{Er}(n, 2n)^{161}\text{Er}$ reaction cross section theoretical calculations

Statistical code	Optical model	Level density model	γ -strength function model
TALYS [16]	Koning-Delaroche [36]	Constant temperature + Fermi gas [41] Back-shifted Fermi gas [42] Generalized superfluid [43,44] 3 microscopic models [45–47]	Brink-Axel [38,39] Kopecky-Uhl [40]
TALYS [16]	Bauge [52]	Microscopic model 3 [47]	Hartree-Fock-Bogolyubov [51]
EMPIRE [17]	Varner [60]	Generalized superfluid model [56]	Lorentzian (MLO1) [58]
EMPIRE [17]	Koning-Delaroche [36]	Generalized superfluid model [56]	Kopecky-Uhl [40]
MECO [18]	Koning-Delaroche [36]	Constant temperature + Fermi gas [41]	Lorentzian [66]

most suitable neutron optical model (OM) potential, extensive tests were carried out using all the available OM potentials for ^{162}Er and the spherical one by Varner *et al.* [60], which was used in this set of calculations; the one from Koning and Delaroche *et al.* [36] seemed to more accurately reproduce the core of the available experimental datasets. A critical factor in the calculations was the determination of the pre-equilibrium emission, for which the multistep direct (MSD) quantum statistical mechanism was invoked as implemented in the code [61], but not the multistep compound (MSC) one. This slight reduction of the pre-equilibrium emission contribution led to a better reproduction of the experimental data over the whole studied energy range.

In the EMPIRE code, calculations were also performed by combining the generalized superfluid model [56] with the optical model of Koning and Delaroche [36] and the Kopecky and Uhl form [40] for the γ -ray strength functions of the $E1$ transition. Moreover, the multistep direct (MSD) quantum statistical mechanism was implemented, in accordance with the multistep compound (MSC) one, in order to take into account the pre-equilibrium emission.

In the MECO code neutron absorption from the ^{162}Er target was calculated with the optical model using the parameters reported by Koning and DeLaroche [36]. The compound nucleus deexcitation was calculated according to the Weisskopf formalism as described in Ref. [18]. The validity of this approximation is justified given that the maximum angular momentum imparted to the compound nucleus does not exceed $5\hbar$. In this compound nucleus spin range the yrast lines of the nuclei involved are fairly flat. Level densities were calculated with the composite formula of Gilbert and Cameron [41]. Excitation energy dependent level density parameters were employed according to the ansatz of Ignatyuk *et al.* [62].

TABLE VI. Measured cross section values for the $^{162}\text{Er}(n, 2n)^{161}\text{Er}$ reaction

Energy (MeV)	σ (barns)
10.7 ± 0.1	0.44 ± 0.08
11.0 ± 0.1	0.57 ± 0.06
11.3 ± 0.1	0.72 ± 0.11
17.1 ± 0.3	1.97 ± 0.22
18.1 ± 0.2	1.84 ± 0.23
19.0 ± 0.2	1.92 ± 0.23

Emission of neutrons, protons and α 's was taken into account with transmission coefficients derived from optical model calculations with global parameters from Refs. [63–65]. Emission of $E1$ γ rays was considered using the Lorentzian strength function of Ref. [66]. Pre-equilibrium neutron emission and fission were not considered.

In Table V the details of the statistical model calculations are presented for the $^{162}\text{Er}(n, 2n)^{161}\text{Er}$ reaction cross section. The different optical model parametrizations, the level density models and the adopted γ -strength functions are given.

V. RESULTS AND DISCUSSION

The experimental data of the $^{162}\text{Er}(n, 2n)^{161}\text{Er}$ reaction, resulting from the present work, are presented in Table VI along with their uncertainties. All the data reported for the near-threshold energies at 10.7–11.3 MeV, as well as for the higher energy region at 17.1–19.0 MeV, are determined for the first time. Both energy regions are of special interest. At near-threshold energies experimental data are needed in order to determine the onset of the reaction cross section. At higher energies the cross section measurements are also interesting since the contribution of the pre-equilibrium mechanism and the $(n, 3n)$ channel to the total neutron absorption reaction cross section become important.

The experimental cross section data are shown in Fig. 4 along with the previous measurements reported in the literature [6–14] and the ENDF/B-VIII.0 evaluation [67]. As can be seen, the previous measurements of the reaction cross section are not only limited in a narrow energy range of 13.5–15.0

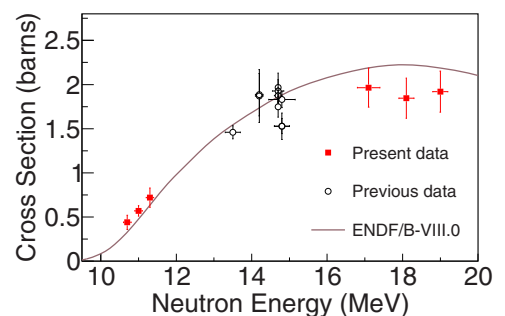


FIG. 4. The experimental $^{162}\text{Er}(n, 2n)^{161}\text{Er}$ cross section values obtained at NCSR “Demokritos” compared with previous experimental data [6–14] and the ENDF/B-VIII.0 [67] evaluation.

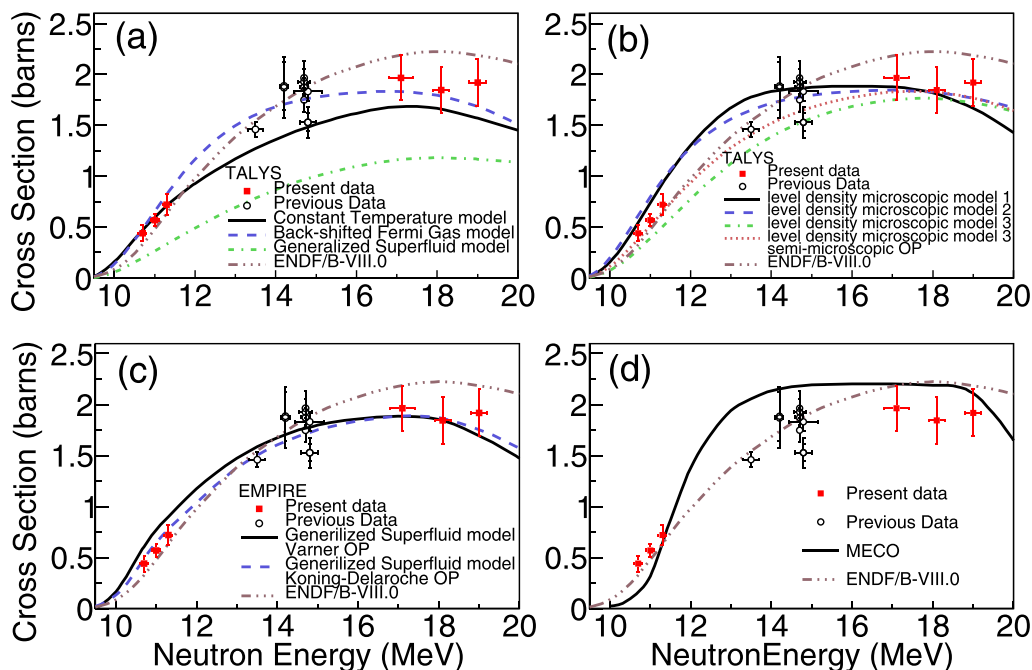


FIG. 5. The experimental $^{162}\text{Er}(n, 2n)^{161}\text{Er}$ cross section values along with the existing data in literature [6–14], the ENDF/B-VIII.0 evaluation [67], and the theoretical calculations obtained with (a)–(b) TALYS [16], (c) EMPIRE [17], and (d) MECO [16] codes.

MeV, but also demonstrate significant discrepancies. Through the present work the mapping of the excitation function over a broad energy region is achieved. By the comparison of the new data with the ENDF/B-VIII.0 [67] theoretical trend, it is concluded that the evaluated cross section values are confirmed from the experimental results at the near-threshold energies of the present work. In contrast, at higher energies the ENDF/B-VIII.0 [67] evaluated cross section values are overestimated by 17%. Accordingly, with the two energy regions of the excitation function covered in the present work, the validation of the theoretical calculations and the corresponding parametrization can be utilized in a more accurate way. The different theoretical trends obtained in the present investigation are presented in Fig. 5.

Specifically, in Fig. 5(a) the results of the theoretical calculations as obtained from the TALYS code are presented. In these calculations global parametrization (Table V) was used for different phenomenological level density models. The results show that the back-shifted Fermi gas model [42] describes quite well the cross section behavior at near-threshold energies, as well as the higher energy part between 17.1 and 19.0 MeV. It also follows the trend of the majority of the previous experimental data between 13.5 and 15 MeV. The behavior of the constant temperature model [41] is less satisfactory. This calculation seems to agree with the data at near-threshold energies. However, it does not reproduce the high energy experimental data of the present work as well as the previous data. On the other hand, the last phenomenological model for the level density parametrization, the generalized superfluid model [43,44], fails to describe the $^{162}\text{Er}(n, 2n)^{161}\text{Er}$ reaction cross section experimental data. In this point, it is important to be mentioned that the effectiveness of the back-shifted Fermi gas model [42] in this mass region is also reported by

Dzysiuik *et al.* [6]. In particular, this level density model is the one that reproduces better the experimental data accrued for the $^{156}\text{Dy}(n, 2n)^{155}\text{Dy}$ reaction. In this mass region, the back-shifted Fermi gas model [42] was also applied by Serris *et al.* [68] for the reproduction of the experimental data of the $^{176}\text{Hf}(n, 2n)^{175}\text{Hf}$ reaction, providing also consistent results.

In Fig. 5(b) the theoretical calculations resulting from the TALYS code are presented, but this time using three microscopic models [45–47] for the level density calculations. Among them the optimal behavior is noticed for the model reported by Goriely *et al.* [46] (microscopic model 2), which describes adequately the energy regions studied in the present work, as well as the previous measurements. Also quite satisfactory is the data reproduction of the microscopic model of Goriely *et al.* [45] (microscopic model 1). The behavior of the microscopic model of Hilaire *et al.* [47] (microscopic model 3) was improved by combining it with the semimicroscopic optical potential of Bauge *et al.* [52] and a microscopic model for the strength functions based on Hartree-Fock-Bogolyubov calculations [51]. This combination of parameters has also been applied in the case of the neutron deficient hafnium isotopes ^{174}Hf and ^{176}Hf [68], and the results were consistent with the experimental data.

Note that among the three phenomenological level density models, the constant temperature model [41] and the back-shifted Fermi gas model [42] that reproduce better the experimental data, seem to be more consistent with the experimental values of the s -wave resonance spacing [55] (Table VII) and the observed discrete levels [54].

Theoretical calculations were also performed with the EMPIRE code, using different models for the optical parametrization, the level density, and the γ -ray strength functions, and the best combination of parameters are given in

TABLE VII. The experimental value of D_0 for ^{163}Er , as obtained from RIPL-2 database [55], compared with the theoretical values predicted for each level density model.

Level density model	Expt. value of D_0 (eV)	Theor. value of D_0 (eV)
Constant temperature [41]	8.00	7.98
Back-shifted Fermi gas [42]	8.00	6.60
Generalized superfluid [43,44]	8.00	1.40
Microscopic 1 [45]	8.00	10.40
Microscopic 2 [46]	8.00	8.00
Microscopic 3 [47]	8.00	8.00

Table V. The obtained theoretical trends, presented in Fig. 5(c), are based on the generalized superfluid model [56] for the level densities. The calculation, which use the optical model of Varner [60] and the modified Lorentzian model [58] for the γ -ray strength functions, reproduces the data fairly well—as well as the previous results—especially at the high energy part of the excitation function, by slightly reducing the contribution of the pre-equilibrium process. A better reproduction of the data at the near-threshold energies is achieved when the Koning and Delaroche optical potential [36] and the Kopecky and Uhl γ -strength functions [40] are used. The last parametrization was applied by Serris *et al.* [68] for the study of the $(n, 2n)$ channel in the ^{174}Hf and ^{176}Hf isotopes, and the results were in good agreement with the experimental data.

It has to be noted that, despite the fact that the GSM model fails in TALYS calculations to reproduce the experimental data,

the different models and parametrization used in the EMPIRE calculations promote finally this level density model.

A final estimation of the $^{162}\text{Er}(n, 2n)^{161}\text{Er}$ excitation function was derived through the MECO code. This calculation is based on global parameters, therefore it should be considered as a prediction and not an adjustment to fit the data. The obtained theoretical trend, which can be seen in Fig. 5(d), follows the general behavior of the experimental data.

In order to investigate the effect of neutron number on the reaction rate of the $(n, 2n)$ channel for all the stable erbium isotopes, a set of theoretical calculations was performed with the TALYS code. For these calculations, the back-shifted Fermi gas level density model [42] was adopted with the model parametrization described in the previous section. The theoretical trends accrued are presented in Fig. 6, along with the ENDF/B-VIII.0 evaluation [67] and the experimental data reported in the literature [69]. From these calculations, we can see that as the neutron number increases, the reaction threshold moves towards lower energies, as expected. The cross section value on the plateau of the theoretically deduced excitation functions for the two neutron deficient erbium isotopes is slightly lower than for the rest of the stable erbium isotopes, while the plateau becomes wider as the mass number is reduced. These theoretical calculations are consistent with the majority of the experimental data, which are available for a few only isotopes and limited to the energy region of 14 MeV.

VI. CONCLUSIONS

The cross section of the $(n, 2n)$ reaction on ^{162}Er has been determined for incident neutron energies in the ranges 10.7–11.3 and 17.1–19.0 MeV, using the activation technique.

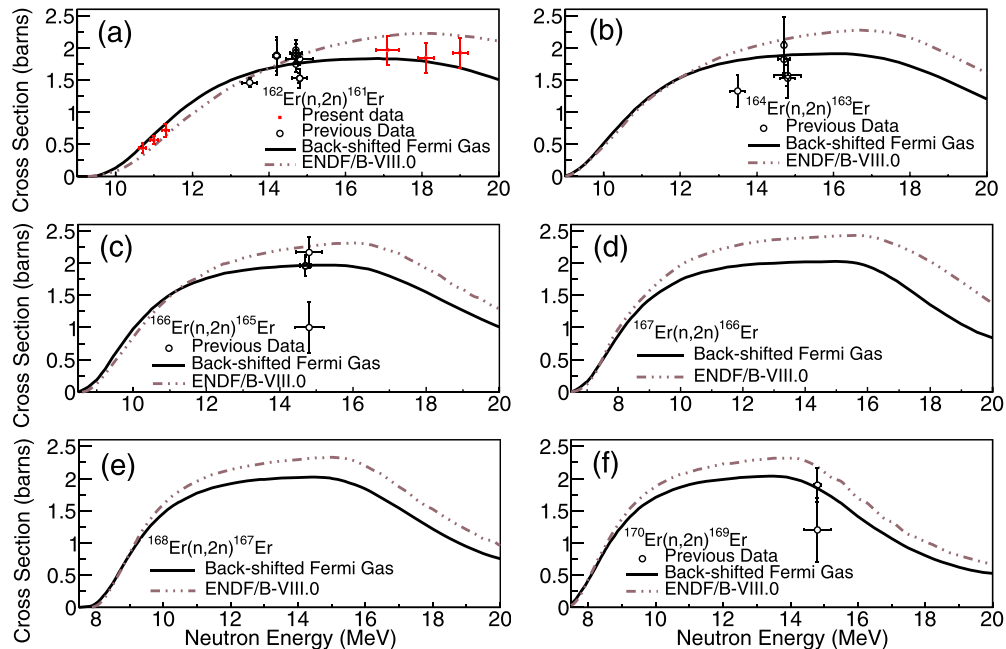


FIG. 6. The theoretical calculations of the $(n, 2n)$ channel for all the stable erbium isotopes, as performed in TALYS code with the back-shifted Fermi gas model [42] for the level densities. The ENDF/B-VIII.0 evaluation [67] and the experimental data of each reaction are presented in the respective plots: (a) $^{162}\text{Er}(n, 2n)^{161}\text{Er}$, (b) $^{164}\text{Er}(n, 2n)^{163}\text{Er}$, (c) $^{166}\text{Er}(n, 2n)^{165}\text{Er}$, (d) $^{167}\text{Er}(n, 2n)^{166}\text{Er}$, (e) $^{168}\text{Er}(n, 2n)^{167}\text{Er}$, (f) $^{170}\text{Er}(n, 2n)^{169}\text{Er}$.

To overcome the problem of the low abundance of ^{162}Er (0.139%) in natural Er, the induced activity was measured by two 100% HPGe detectors in close geometry in order to increase the detection efficiency of the system. To avoid summing-up effects in the Ge crystals during the efficiency calibration procedure, a weak monoenergetic ^{54}Mn source was used, which emits an 835 keV γ ray, very close to the 826.6 keV energy of the strongest decay line of ^{161}Er .

Statistical model calculations with the broadly used statistical codes TALYS and EMPIRE, along with the code MECO, were performed. In the TALYS code the behavior of the excitation function was investigated as a function of the level density models provided by the code. Among them the back-shifted Fermi gas model [42] and the two microscopic models suggested by Goriely *et al.* [45] (microscopic model 1) and Goriely *et al.* [46] (microscopic model 2) reproduce better the experimental data. The microscopic model of Hilaire *et al.* [47] has a better behavior when is combined with the semimicroscopic potential of Bauge *et al.* [52] and Hartree-Fock-Bogolyubov calculations [51] for the γ -ray strength function. On the other hand, in the calculations using the EMPIRE code, implementing the generalized superfluid model [56] for the level density calculations, a better reproduction of the data was achieved. The calculations were improved when the generalized superfluid model [56] was applied in combination with the optical potential of Koning and Delaroche [36] and the Kopecky and Uhl model [40] for the γ -ray strength functions. The same combinations of parameters used in TALYS and EMPIRE codes for the reproduction of the $^{162}\text{Er}(n, 2n)^{161}\text{Er}$

reaction cross section have also been applied in the cases of $^{174}\text{Hf}(n, 2n)^{173}\text{Hf}$ and $^{176}\text{Hf}(n, 2n)^{155}\text{Hf}$ data [68], and the theoretical results were in good agreement with experimental measurements. Finally, the theoretical trend resulted from the MECO code also follows the general trend of the experimental data.

In conclusion, within the present work the $^{162}\text{Er}(n, 2n)^{161}\text{Er}$ reaction cross section was studied experimentally and theoretically from the reaction threshold up to the 19 MeV neutron beam energy. The present experimental data along with the previous results were compared with different theoretical calculations. The present research activity should also be extended in other neutron deficient nuclei in this mass region given that the existing experimental information is limited. In this way a more systematic investigation with respect to the performance of the theoretical calculations can be achieved.

ACKNOWLEDGMENTS

The authors would like to acknowledge the assistance of the accelerator staff at NCSR “Demokritos,” namely M. Andrianis and V. Andreopoulos. We also acknowledge support of this work by the project “CALIBRA/EYIE” (MIS 5002799) which is implemented under the Action “Reinforcement of the Research and Innovation Infrastructure,” funded by the Operational Programme “Competitiveness, Entrepreneurship and Innovation” (NSRF 2014–2020) and cofinanced by Greece and the European Union (European Regional Development Fund).

-
- [1] M. Salvatores and G. Palmiotti, *Prog. Part. Nucl. Phys.* **66**, 144 (2011).
- [2] Douglas E. Burkens, Randall S. Fielding, and Douglas L. Porter, *J. Nucl. Mater.* **392**, 158 (2009).
- [3] S. W. Kuk, K. H. Kim, J. H. Kim, H. Song, S. J. Oh, J.-Y. Park, C. B. Lee, Y.-S. Youn, and J.-Y. Kim, *J. Nucl. Mater.* **486**, 53 (2017).
- [4] N. Kodochigov, Yu. Sukharev, E. Marova, N. Ponomarev-Stepnoy, E. Glushkov, and P. Fomichenko, *Nucl. Eng. Design* **222**, 161 (2003).
- [5] K. Shibata, *J. Nucl. Sci. Technol.* **49**, 824 (2012).
- [6] N. Dzysiuk, A. Kadenko, I. Kadenko, and G. Primenko, *Phys. Rev. C* **86**, 034609 (2012).
- [7] J. Luo, R. Liu, L. Jiang, and Z. Liu, *J. Radioanal. Nucl. Chem.* **289**, 455 (2011).
- [8] X. Kong, Y. Wang, and J. Yang, *Appl. Radiat. Isotopes* **49**, 1529 (1998).
- [9] N. Lakshmana Das, C. V. Srinivasa Rao, B. V. Thirumala Rao, and J. Rama Rao, *Pramana - J. Phys.* **17**, 99 (1981).
- [10] H. Liljavirta and T. Tuurnala, *Phys. Scr.* **18**, 75 (1978).
- [11] S. M. Qaim, *Nucl. Phys. A* **224**, 319 (1974).
- [12] A. Bari, *Dissertation Abstracts B (Sciences)* **32**, 5091 (1972).
- [13] E. Havlik, *Acta Physica Austriaca* **34**, 209 (1971).
- [14] P. Rama Prasad, J. Rama Rao, and E. Kondaiiah, *Nucl. Phys. A* **125**, 57 (1969).
- [15] J. K. Tuli, *Nuclear Wallet Cards*, October 2011, National Nuclear Data Center, <https://www.nndc.bnl.gov>
- [16] A. J. Koning, S. Hilaire, and M. C. Duijvestijn, TALYS-1.0, in *Proceedings of the International Conference on Nuclear Data for Science and Technology*, April 22–27, 2007, Nice, France, edited by O. Bersillon, F. Gunsing, E. Bauge, R. Jacqmin, and S. Leray (EDP Sciences, Les Ulis, France, 2008), pp. 211–214.
- [17] M. Herman, R. Capote, B. Carlson, P. Oblozinsky, M. Sin, A. Trkov, H. Wienke, and V. Zerkin, *Nucl. Data Sheets* **108**, 2655 (2007), special issue on evaluations of neutron cross sections.
- [18] N. G. Nicolis, *Int. J. Mod. Phys. E* **17**, 1541 (2008).
- [19] International Reactor Dosimetry and Fusion File IRDFF v.1.05, 09 October 2014 <https://www-nds.iaea.org/IRDFF/>; R. Capote, K. I. Zolotarev, V. G. Pronyaev, and A. Trkov, *J. ASTM Int.* **9**, 104119 (2012); E. M. Zsolnay, R. Capote, H. K. Nolthenius, and A. Trkov, IAEA Technical Report INDC(NDS)-0616, 2012.
- [20] G. Vourvopoulos, T. Paradellis, and A. Asthenopoulos, *Nucl. Instrum. Methods Phys. Res.* **220**, 23 (1984).
- [21] E. Birgersson and G. Lovestam, JRC Science Hub Technical Report, Ref. No. 23794, 2009.
- [22] J. F. Ziegler, J. P. Biersack, and M. D. Ziegler, SRIM-2013, available at <http://www.srim.org>
- [23] P. Grigoriadou, M. Kokkoris, N. Patronis, and R. Vlastou, in *Proceedings of the HNPS symposium*, University of Ioannina, Ioannina 22–23 May 2015, http://hnps2015.physics.uoi.gr/Files/Book_Proc_HNPS2015.pdf
- [24] A. Kalamara, R. Vlastou, M. Kokkoris, M. Diakaki, A. Tsinganis, N. Patronis, M. Axiotis, and A. Lagoyannis, *Phys. Rev. C* **93**, 014610 (2016).

- [25] X-5 Monte Carlo team, MCNP-A General Monte Carlo N-Particle Transport Code, version 5, Volumes I–III, LA-UR-03-1987, LA-CP-03-0245 and LA-CP-03-0284, April 2003.
- [26] C. W. Reich, *Nucl. Data Sheets* **112**, 2497 (2011).
- [27] K. Debertin and R. G. Helmer, *Gamma- and X-Ray Spectrometry with Semiconductor Detectors* (North-Holland, Amsterdam, 2008).
- [28] S. Agostinelli *et al.*, *Nucl. Instrum. Methods. Phys. Res. A* **506**, 250 (2003); J. Allison *et al.*, *IEEE Trans. Nucl. Sci.* **53**, 270 (2006); *Nucl. Instrum. Methods. Phys. Res. A* **835**, 186 (2016).
- [29] Y. Dong and H. Junde, *Nucl. Data Sheets* **121**, 1 (2014).
- [30] M. J. Martin, *Nucl. Data Sheets* **114**, 1497 (2013).
- [31] R. B. Firestone, *Nucl. Data Sheets* **108**, 2319 (2007).
- [32] H. Xiaolong, *Nucl. Data Sheets* **108**, 1093 (2007).
- [33] C. M. Baglin, *Nucl. Data Sheets* **113**, 2187 (2012).
- [34] H. Beer and F. Käppeler, *Phys. Rev. C* **21**, 534 (1980).
- [35] W. Hauser and H. Feshbach, *Phys. Rev.* **87**, 366 (1952).
- [36] A. J. Koning and J. P. Delaroche, *Nucl. Phys. A* **713**, 231 (2003).
- [37] A. J. Koning and M. C. Duijvestijn, *Nucl. Phys. A* **744**, 15 (2004).
- [38] D. M. Brink, *Nucl. Phys.* **4**, 215 (1957).
- [39] P. Axel, *Phys. Rev.* **126**, 671 (1962).
- [40] J. Kopecky and M. Uhl, *Phys. Rev. C* **41**, 1941 (1990).
- [41] A. Gilbert and A. G. W. Cameron, *Can. J. Phys.* **43**, 1446 (1965).
- [42] W. Dilg, W. Schantl, H. Vonach, and M. Uhl, *Nucl. Phys. A* **217**, 269 (1973).
- [43] A. V. Ignatyuk, K. K. Istekov, and G. N. Smirenkin, *Sov. J. Nucl. Phys.* **29**, 450 (1979).
- [44] A. V. Ignatyuk, J. L. Weil, S. Raman, and S. Kahane, *Phys. Rev. C* **47**, 1504 (1993).
- [45] S. Goriely, F. Tondeur, and J. M. Pearson, *At. Data Nucl. Data Tables* **77**, 311 (2001).
- [46] S. Goriely, S. Hilaire, and A. J. Koning, *Phys. Rev. C* **78**, 064307 (2008).
- [47] S. Hilaire, M. Girod, S. Goriely, and A. J. Koning, *Phys. Rev. C* **86**, 064317 (2012).
- [48] M. K. Grossjean and H. Feldmeier, *Nucl. Phys. A* **444**, 113 (1985).
- [49] P. Demetriou and S. Goriely, *Nucl. Phys. A* **695**, 95 (2001).
- [50] V. Martin, J. L. Egidio, and L. M. Robledo, *Phys. Rev. C* **68**, 034327 (2003).
- [51] R. Capote, M. Herman, P. Obložinsky, P. G. Young, S. Goriely, T. Belgia, A. V. Ignatyuk, A. J. Koning, S. Hilaire, V. Plujko, M. Avrigeanu, O. Bersillon, M. B. Chadwick, T. Fukahori, S. Kailas, J. Kopecky, V. M. Maslov, G. Reffo, M. Sin, E. Soukhovitskii, P. Talou, H. Yinlu, and G. Zhigang, *Nucl. Data Sheets* **110**, 3107 (2009).
- [52] E. Bauge, J. P. Delaroche, and M. Girod, *Phys. Rev. C* **63**, 024607 (2001).
- [53] A. J. Koning, S. Hilaire, and S. Goriely, *Nucl. Phys.* **810**, 13 (2008).
- [54] R. Capote *et al.*, <https://www-nds.iaea.org/RIPL-3/>, 2009.
- [55] T. Belgia *et al.*, <https://www-nds.iaea.org/RIPL-2/>, 2006.
- [56] A. D. Arrigo, G. Giardina, M. Herman, A. Ignatyuk, and A. Taccone, *J. Phys. G* **20**, 365 (1994).
- [57] H. Hofmann, J. Richert, J. Tepel, and H. Weidenmüller, *Ann. Phys. (N.Y.)* **90**, 403 (1975).
- [58] V. A. Plujko, *Acta Phys. Pol. B* **31**, 435 (2000).
- [59] V. Avrigeanu, P. E. Hodgson, and M. Avrigeanu, *Phys. Rev. C* **49**, 2136 (1994).
- [60] R. L. Varner, W. J. Thompson, T. L. McAbee, E. J. Ludwig, and T. B. Clegg, *Phys. Rep.* **201**, 57 (1991).
- [61] T. Tamura, T. Udagawa, and H. Lenske, *Phys. Rev. C* **26**, 379 (1982).
- [62] A. V. Ignatyuk *et al.*, *Sov. J. Nucl. Phys.* **29**, 255 (1975).
- [63] D. Wilmore and P. E. Hodgson, *Nucl. Phys.* **55**, 673 (1964).
- [64] C. M. Perey and F. G. Perey, *Nucl. Data Tables* **17**, 1 (1976).
- [65] J. R. Huizenga and G. Igo, *Nucl. Phys.* **29**, 462 (1962).
- [66] A. S. Iljinov *et al.*, *Nucl. Phys. A* **543**, 517 (1992).
- [67] <https://www.nndc.bnl.gov/exfor/endlf00.jsp>
- [68] M. Serris, M. Diakaki, S. Galanopoulos, M. Kokkoris, M. Lamprou, C. T. Papadopoulos, R. Vlastou, P. Demetriou, C. A. Kalfas, and A. Lagoyannis, *Phys. Rev. C* **86**, 034602 (2012).
- [69] <https://www-nds.iaea.org/exfor/exfor.htm>.